

# Memory-Efficient 2D/3D Shape Assembly of Robot Swarms

Shuoyu Yue, Pengpeng Li, Yang Xu, Kunrui Ze, Xingjian Long, Huazi Cao, Guibin Sun

**Abstract**—Mean-shift-based approaches have recently emerged as the most effective methods for robot swarm shape assembly tasks. These methods rely on image-based representations of target shapes to compute local density gradients and perform mean-shift exploration, which constitute their core mechanism. However, such image representations incur substantial memory overhead, which can become prohibitive for high-resolution or 3D shapes. To overcome this limitation, we propose a memory-efficient tree map representation that hierarchically encodes user-specified shapes and is applicable to both 2D and 3D scenarios. Building on this representation, we design a behavior-based distributed controller that enables assignment-free shape assembly. Comparative 2D and 3D simulations against a state-of-the-art mean-shift algorithm demonstrate one to two orders of magnitude lower memory usage and two to three times faster shape entry while maintaining comparable uniformity. Finally, we validate the framework through physical experiments with 6 to 7 UAVs, confirming its real-world practicality.

**Index Terms**—Shape assembly, robot swarms, tree mapping.

## I. INTRODUCTION

**I**N nature, insect groups can assemble into functional structures through purely local interactions [1]. For instance, fire ants dynamically build living bridges to span gaps and transport resources, with stability emerging from simple individual rules. Inspired by such collective behaviors, swarm robotics are extensively explored as a means for large groups of robots to self-organize into desired 2D or 3D configurations, enabling applications from cooperative construction to search-and-rescue in complex environments [2]–[7].

Existing swarm shape assembly methods can be categorized into assignment-based and assignment-free paradigms. Assignment-based methods allocate robots to target positions either through centralized optimization [8], [9] or through distributed coordination. The latter can be achieved by rule-based methods (e.g., local constraints and negotiation protocols) [10]–[14] or learning-based methods [15]. Centralized schemes provide globally consistent solutions but suffer from poor scalability as swarm size increases and are highly vulnerable to individual failures [6]. Distributed schemes address these limitations by decomposing the centralized assignment into multiple local ones, but conflicts can arise from concurrent local decisions and require additional techniques like task

This work was supported by National Key Laboratory of Multi-perch Vehicle Driving Systems under Grant QDXT-NZ-202407-01. (Corresponding authors: Kunrui Ze; Guibin Sun.)

Shuoyu Yue is with the Cavendish Laboratory, University of Cambridge, Cambridge CB3 0HE, United Kingdom (e-mail: shuoyu.yue@gmail.com). This work was conducted during his research internship at Beihang University.

Pengpeng Li is with the School of Artificial Intelligence; Yang Xu, Kunrui Ze, Xingjian Long, and Guibin Sun are with the School of Automation Science and Electrical Engineering, Beihang University, Beijing 100191, China (e-mail: {pengpengli, xuyangx, kr\_ze, longxj, sunguibinx}@buaa.edu.cn).

Huazi Cao is with the Westlake Institute for Optoelectronics, Fuyang, Hangzhou, Zhejiang 311421, China (e-mail: caohuazi@wioe.westlake.edu.cn).

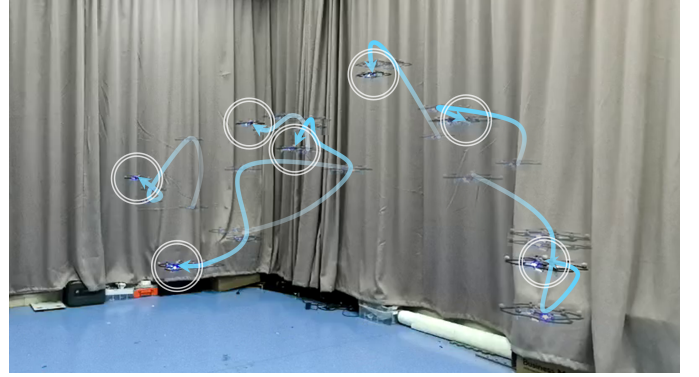


Fig. 1. Physical experiment with 7 UAVs forming a 3D arrow. Final UAV positions are marked with white circles. Trajectories are shown as smooth blue curves passing through five sampled positions for each UAV, with color gradually deepening with time. Note that the curves depict smoothed connections rather than exact flight paths.

swapping [16] to ensure consistency. In contrast, assignment-free approaches avoid explicit goal allocation and instead exploit emergent behaviors, such as edge growth from seed robots [17], morphogenetic pattern formation [18], artificial potential fields [19], and saliency-driven filling [20]. More recently, image-based approaches have been explored, with mean-shift exploration strategies becoming the state-of-the-art solutions for large-scale swarm shape assembly [21], [22]. Advances in distributed relative localization further support their practical deployment [23]. These methods have been shown to outperform earlier assignment-free approaches in coverage speed and robustness in 2D scenarios [21]. However, the reliance on image maps causes memory demand to grow rapidly with resolution, making direct extension to 3D prohibitively expensive.

Whether assignment-based or assignment-free, most existing methods remain confined to 2D assemblies, and scalable 3D extensions remain rare and technically demanding. For aerial swarms, Morgan et al. proposed a distributed auction algorithm with trajectory planning [8], yet it entails substantial memory and communication costs as each robot must store all target points and iteratively exchange bids. Underwater bio-inspired swarms exhibit 3D patterns via visual signaling [24], but the results are coarse, transient behaviors rather than precisely-defined shapes. Other studies focus on physical 3D construction, including layered aerial robotic block assembly [25], self-climbing assembly (FireAnt3D) [26], shape-changing modular tensegrity blocks [27], and snap-together soft robots (SoftSnap) [28]. However, these approaches typically grow buildings sequentially from fixed bases or seed robots, thus differing fundamentally from the free-space shape assembly problem addressed in this study.

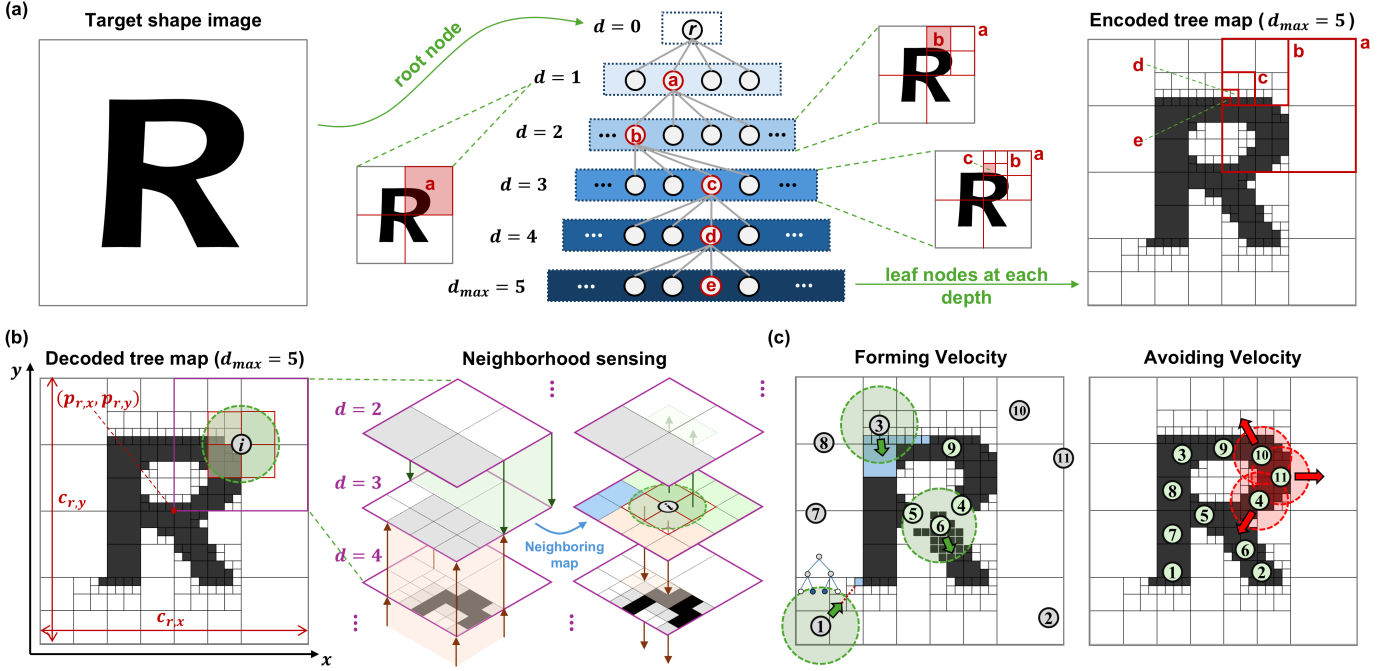


Fig. 2. Overview of the Proposed Framework. (a) Shape encoding: The target shape image is shown on the left, while the middle and right panels depict the encoded tree map as a tree structure and a grid view, respectively. A complete encoding path from node  $a$  at  $d = 1$  to node  $e$  at  $d_{\max} = 5$  is highlighted in red in both the tree structure and the grid view. (b) Shape decoding: Physical lengths are assigned to the root node  $r$ , and thus to the entire tree map. A neighboring map is established at  $d = 3$  and used for each robot  $i$  to perceive its neighborhood. The sensing range of robot  $i$  is shown as a green circle and the sensed neighborhood is outlined in red. (c) Shape assembly controller: Examples of the two velocity commands under different cases are illustrated. The collision-avoidance range of each robot is shown as a red circle.

In this letter, we propose a memory-efficient, assignment-free shape assembly framework for large-scale robot swarms applicable to both 2D and 3D settings. Specifically, we first encode the user-specified target shape into a tree map, which substantially reduces memory requirements. Based on this map, we design a behavior-based distributed shape assembly controller. We validate the framework through extensive 2D and 3D simulations, which demonstrate reliable formation of complex shapes. Compared with a state-of-the-art method [21], our approach reduces memory usage by one to two orders of magnitude and improves shape-entering efficiency by a factor of two to three, while maintaining comparable uniformity. Finally, we confirm the practical feasibility of the proposed method through physical experiments using UAVs.

## II. METHODOLOGY

In this section, we tackle the challenge of representing and using the target shape image as a map for swarm shape assembly while keeping memory usage low, especially in 3D. We introduce a tree-based encoding-decoding method that converts a dense target image into a coarse, hierarchical tree map. Based on this map, we design a distributed, assignment-free assembly controller with forming and collision-avoidance velocities. An overview is given in Fig.2.

### A. Shape Encoding

The target shape encoding is shown in Fig. 2(a), where a user-specified binary image is converted into a tree map. For clarity, all figures in this section use 2D examples. Since

the method applies to both 2D and 3D, we use  $\lambda$  to indicate dimensionality in the following descriptions. The maximum tree depth  $d_{\max}$  controls the map resolution and memory cost, with  $d_{\max} = 5$  for all examples in Fig. 2.

The encoding is performed in a breadth-first search manner. A root node  $r$ , representing the entire image, is first created at depth  $d = 0$ . This node is then subdivided into  $n_{\text{div}} = 2^\lambda$  equal child nodes, which form layer 1 ( $d = 1$ ) of the tree. For each node in this layer, the pixels it contains are examined. If all pixels are of the same color (black or white), the node is marked as a leaf node of that color. Otherwise, it is further divided into  $2^\lambda$  child nodes, which are placed in layer 2. After all nodes in layer 1 are processed, the algorithm proceeds to layer 2 and is repeated until  $d = d_{\max}$ . For any node at depth  $d_{\max}$  that still contains pixels of different colors, it is assigned as a black leaf node if the majority of its pixels are black, and as a white leaf node otherwise. Fig. 2(a) shows an example: node  $a$  at layer 1 contains pixels of different colors, so it is subdivided into four child nodes, including node  $b$  at layer 2. Then node  $b$  is further divided into four child nodes, including node  $c$  at layer 3.

The judgment at depth  $d_{\max}$  may result in all child nodes of a parent having the same color, which leads to redundant memory usage. To address this issue, a merging step is applied after the tree generation. In this step, all parent nodes are iteratively examined. If all child nodes of a parent are leaf nodes with the same color, they are removed, and the parent is converted into a leaf node. This procedure is repeated until no further merging is possible. As illustrated on the right of

Fig. 2(a), the final output is a coarse tree map whose leaf nodes serve as map cells. Since the colors of leaf nodes are  $\rho \in \{0, 1\}$ , the map is black and white. Moreover, because the leaf nodes reside in different layers and have varying sizes, the map is inherently heterogeneous. The memory usage  $m_{\text{tree}}$  of a tree map is computed as

$$m_{\text{tree}} = n_{\text{div}}m_{\text{link}} + n_{\text{middle}}(n_{\text{div}} + 1)m_{\text{link}} + n_{\text{leaf}}(m_{\text{link}} + m_{\text{color}}). \quad (1)$$

Here, the first term accounts for the root node, while  $n_{\text{middle}}$  and  $n_{\text{leaf}}$  denote the numbers of middle-layer and leaf nodes, respectively. The parameter  $m_{\text{link}}$  represents the memory required for a unidirectional link between a parent and a child node. Each link is stored as an integer node index occupying 4 bytes, which is sufficient for all 2D and 3D shapes and resolutions considered in this study. The parameter  $m_{\text{color}}$  corresponds to the memory occupied by a single color value. Since the color values in a tree map are binary,  $m_{\text{color}}$  is set to one bit. By contrast, the method in [21] employs a full-grid map, where a grayscale gradient field is constructed from the original image to guide robots into the target shape. The memory required for a full-grid map is

$$m_{\text{full-grid}} = n_{\text{cell}} \times m_{\text{color}}, \quad (2)$$

where  $n_{\text{cell}}$  is the total number of cells and  $m_{\text{color}}$  is 4 bytes for a single-precision floating-point number since  $\rho \in [0, 1]$  in this case.

### B. Shape Decoding and Robot Localization

In decoding, each node  $n$  in the tree is associated with physical quantities, namely its center position  $\mathbf{p}_n \in \mathbb{R}^\lambda$  and size  $\mathbf{c}_n \in \mathbb{R}^\lambda$ . An example for the root node  $r$  is shown in Fig. 2(b) (left). This is achieved by establishing a global coordinate frame and redefining the pixel size in the target shape image. Since robots are intended to occupy the black region, we define the pixel size as

$$c_{\text{pixel}} = \sqrt[\lambda]{\frac{s_r \times n_{\text{robot}}}{n_{\text{black}}}},$$

where  $n_{\text{robot}}$  and  $n_{\text{black}}$  denote the numbers of robots and black pixels, respectively.  $s_r$  represents the space occupied by each robot, approximated in 2D by a circle of radius  $r_{\text{avoid}}/2$ , where  $r_{\text{avoid}}$  is the collision-avoidance distance between robots. In 3D, the footprint generalizes to an ellipsoid with a  $z$ -direction elongation to compensate for the downwash effects. Further details on the downwash compensation are given in Eq. (5) for the avoiding velocity. In addition, we define the attraction  $\beta_n$  of each node  $n$  to a robot, which facilitates the tree search procedure in the controller. The attraction is computed in a bottom-up manner: for a leaf node,  $\beta_n$  is set to its color, whereas for a parent node,  $\beta_n$  is given by the average of the attractions of its child nodes. By this definition,  $\beta_n \in [0, 1]$ , with larger values indicating stronger attraction.

Once the tree map is physically decoded, each robot  $i$  can be localized within the map. Two types of localization are considered depending on the target. The first associates robot  $i$  with a leaf node  $l_i$ . This is performed through a top-down

search: starting from the root node  $r$ , the robot's position  $\mathbf{p}_i$  is compared with the center  $\mathbf{p}_r$  to select the corresponding child node at depth  $d = 1$ . This procedure is repeated at each depth until a leaf node is reached. The second type localizes robot  $i$  at a specified depth. The procedure is the same as the first one but terminates once the target depth is reached. If the target depth exceeds the actual depth of the leaf nodes, virtual child nodes can be temporarily generated to complete the search and released after use.

To enable shape assembly control, each robot  $i$  must sense its neighborhood in the map, focusing on the black cells. This is nontrivial in a tree map because spatial adjacency is partially lost during encoding: cells that appear adjacent in the grid view may correspond to leaf nodes far apart in the tree. To recover this information, we build a full-grid neighboring map at depth  $d_{\text{map}}$  during decoding and use it for control. This map fully overlaps the tree map at  $d = d_{\text{map}}$  and stores all data needed for neighborhood sensing. Fig. 2(b) illustrates this process, where only the top-right quarter is shown for clarity. We set  $d_{\text{map}} = d_{\text{max}} - 2$  (thus  $d_{\text{map}} = 3$  here) for reasons discussed later in this subsection.

Fig. 2(b) (middle) visualizes the focused region of the tree map at depths  $d = 2, 3, 4$ : black/white cells denote leaf nodes, and gray cells are parents that are further divided. The core idea is to construct a full grid at  $d = 3$ , linking each cell to the corresponding leaf nodes. The neighboring map contains three types of cells: (i) overlapping leaf nodes at  $d = 3$ , (ii) overlapping parent nodes at  $d = 3$ , and (iii) lying inside larger leaf nodes at shallower depths. Cells of types (i) and (iii) directly link to their leaf nodes regardless of size, whereas type (ii) cells record only the overlapped parent node and traverse its subtree (two layers deep) on demand to retrieve all child leaf nodes. Linking of types (ii) and (iii) is highlighted in red and green in Fig. 2(b).

The resulting neighboring map is shown in Fig. 2(b) (right), with cells of types (i)-(iii) marked in blue, red, and green, respectively. To use this map, robot  $i$  is localized to  $d_{\text{map}}$  first, and the neighboring cells within its sensing range  $r_{\text{sense}}$  (outlined in red) are identified. The linked leaf nodes of these cells are then retrieved according to cell type and sent back to robot  $i$ , allowing it to perceive all surrounding leaf nodes and select the black ones for subsequent steps. The choice of  $d_{\text{map}}$  balances memory and computation: a deeper  $d_{\text{map}}$  creates more cells, making map generation and storage costly, while a shallower  $d_{\text{map}}$  requires deeper subtree traversals for type (ii) cells at each control iteration. In this study, we choose  $d_{\text{map}} = d_{\text{max}} - 2$  as a practical compromise between memory cost and efficiency.

### C. Shape Assembly Controller

The behavior-based distributed controller for robot swarm shape assembly is designed based on the tree map. The control command of robot  $i$  is given in the form of a velocity vector as follows:

$$\mathbf{v}_i = \mathbf{v}_i^{\text{form}} + \mathbf{v}_i^{\text{avoid}},$$

which consists of two components: a forming velocity that drives the robot to assemble the target shape, and an avoiding

velocity that ensures collision avoidance. Fig. 2(c) provides a 2D illustration of the velocity commands.

1) *Forming Velocity*: The forming velocity is designed based on node search within the tree map. The definition of the forming velocity  $\mathbf{v}_i^{\text{form}}$  for robot  $i$  is given as below:

$$\mathbf{v}_i^{\text{form}} = \kappa_1 \frac{\sum_{n \in \mathcal{N}_i} \omega_n (\mathbf{p}_n - \mathbf{p}_i)}{\sum_{n \in \mathcal{N}_i} \omega_n}, \quad (3)$$

where  $\mathbf{p}_n$  and  $\mathbf{p}_i$  denote the center position of node  $n$  and the current position of robot  $i$ , respectively. The set  $\mathcal{N}_i$  contains all the candidate nodes for robot  $i$ , the parameter  $\omega_n$  denotes the weight assigned to each node  $n \in \mathcal{N}_i$ , and  $\kappa_1$  is a positive control gain.

During shape assembly, the role of the controller depends on the robot's relative state with respect to the target shape. When a robot is outside or far from the target region, the controller prioritizes efficient guidance into the shape. Once the robot is near or within the shape, the focus shifts toward filling the shape and achieving a uniform distribution. Accordingly, different node search strategies are applied, leading to distinct definitions of  $\mathcal{N}_i$ . To quantify this relative state for each robot  $i$ , we introduce a parameter  $\eta_i$  as below:

$$\eta_i = \min_{n \in \mathcal{N}_i^{\text{sense}}} \|2(\mathbf{p}_n - \mathbf{p}_i) \oslash \mathbf{c}_n\|_\infty, \quad (4)$$

where  $\oslash$  denotes an element-wise division and  $\mathbf{c}_n$  is the size of node  $n$ . The set  $\mathcal{N}_i^{\text{sense}}$  contains all black leaf nodes within distance  $r_{\text{sense}}$  of robot  $i$ . It is obtained with the neighboring map and is highlighted in blue for robot 3 in Fig. 2(c). The parameter  $\eta_i$  quantifies the relative proximity of robot  $i$  to the shape: the robot is inside the shape if  $\eta_i \leq 1$  and outside otherwise, with  $\eta_i \gg 1$  if  $|\mathcal{N}_i^{\text{sense}}| = 0$ . Based on this parameter, the full candidate set  $\mathcal{N}_i$  is defined as follows:

$$\mathcal{N}_i = \begin{cases} \mathcal{N}_i^{\text{tree}} \cup \mathcal{N}_i^{\text{sense}}, & \eta_i > 1, \\ \mathcal{N}_i^{\text{virtual}}, & \eta_i \leq 1, \end{cases}$$

where  $\mathcal{N}_i^{\text{tree}}$  and  $\mathcal{N}_i^{\text{virtual}}$  are candidate sets obtained with different searching methods.

The set  $\mathcal{N}_i^{\text{tree}}$  contains a leaf node identified through a tree search. Two distinct scenarios are considered for the tree search. First, if robot  $i$  is inside the map but outside the target shape (e.g., robot 1 in Fig. 2(c)), the search starts from the parent node of its current leaf node  $l_i$  and proceeds downward, selecting at each depth the child node with the maximum attraction  $\beta_n$ , until a black leaf node is reached, which is highlighted in blue in Fig. 2(c). Second, if robot  $i$  is outside the map, the search begins from the root node and, at each depth, selects the nearest child node with  $\beta_n > 0$ , continuing downward until a leaf node is reached.

The set  $\mathcal{N}_i^{\text{virtual}}$  consists of virtual nodes defined on an exploration layer at depth  $d_{\text{max}}$ . These virtual nodes are generated dynamically through a subdivision strategy and removed afterward, thereby incurring no additional memory overhead. For each robot  $i$ , localization is performed at depth  $d_{\text{max}}$ , and a uniform grid of virtual nodes is generated within its sensing range  $r_{\text{sense}}$ . The color of each virtual node is then determined by checking whether it lies within a black leaf node in  $\mathcal{N}_i^{\text{sense}}$ . Then the virtual nodes occupied by each neighboring robot

---

### Algorithm 1 Compute Forming Velocity

---

```

1: Input:  $T$ : Tree map,  $P$ : Robot positions
2: if robot  $i$  is outside  $T$  then
3:   Select  $\mathcal{N}_i^{\text{tree}}$  by tree search
4:    $\mathcal{N}_i \leftarrow \mathcal{N}_i^{\text{tree}}$ 
5: else
6:   Select  $\mathcal{N}_i^{\text{tree}}$  by tree search
7:   Select  $\mathcal{N}_i^{\text{sense}}$  with the neighboring map
8:   Compute  $\eta_i$  with  $\mathcal{N}_i^{\text{sense}}$  by Eq. (4)
9:   if  $\eta_i > 1$  then
10:     $\mathcal{N}_i \leftarrow \mathcal{N}_i^{\text{tree}} \cup \mathcal{N}_i^{\text{sense}}$ 
11:   else
12:    Generate  $\mathcal{N}_i^{\text{virtual}}$  using  $\mathcal{N}_i^{\text{sense}}$  and  $\mathcal{N}_i^{\text{robot}}$ 
13:     $\mathcal{N}_i \leftarrow \mathcal{N}_i^{\text{virtual}}$ 
14:   end
15: end
16: Compute  $\mathbf{v}_i^{\text{form}}$  with  $\mathcal{N}_i$  by Eq. (3)

```

---

$j \in \mathcal{N}_i^{\text{robot}}$  are excluded, and the remaining black virtual nodes constitute  $\mathcal{N}_i^{\text{virtual}}$ . Here,  $\mathcal{N}_i^{\text{robot}}$  contains all the neighboring robots located within  $r_{\text{sense}}$  of robot  $i$ , and a virtual node is considered occupied if its distance to any neighboring robot is less than  $r_{\text{avoid}}/2$ . An example of  $\mathcal{N}_i^{\text{virtual}}$  for robot 6 is illustrated in Fig. 2(c).

The weight  $\omega_n$  in Eq. (3) is defined as  $s_n / \|\mathbf{p}_n - \mathbf{p}_i\|$  for  $\eta_i > 1$ , where  $s_n$  denotes the area or volume of candidate node  $n$ . The factor  $s_n$  is included in this regime because the candidate set consists of leaf nodes of varying sizes. In contrast, when  $\eta_i \leq 1$ , all virtual nodes are of equal size, and thus the weight depends solely on the distance. Here,  $\omega_n$  is computed using a function  $\phi(\|\mathbf{p}_n - \mathbf{p}_i\|/r_{\text{sense}})$ , where  $\phi(x)$  is defined as

$$\phi(x) = \begin{cases} 1, & x \leq 0, \\ \frac{1}{2} [1 + \cos(\pi x)], & x \in (0, 1), \\ 0, & x \geq 1. \end{cases}$$

The overall procedure for computing the forming velocity of robot  $i$  is summarized in Algorithm 1.

2) *Avoiding Velocity*: This velocity command is designed to prevent collisions between robots. In 3D robot swarms, the downwash effect must be considered. Downwash refers to the downward airflow generated by UAV propellers, which can destabilize robots flying beneath them. To mitigate this effect, the avoidance distance in the vertical direction is set larger than that in the horizontal directions. The avoidance velocity  $\mathbf{v}_i^{\text{avoid}}$  for robot  $i$  is defined as

$$\mathbf{v}_i^{\text{avoid}} = \sum_{j \in \mathcal{N}_i^{\text{robot}}} \kappa_2 \mu \left( \frac{\|\mathbf{p}_i - \mathbf{p}_j\|}{(1 + \alpha)r_{\text{avoid}}} \right) (\mathbf{p}_i - \mathbf{p}_j), \quad (5)$$

where  $\mathbf{p}_j$  is the position of a neighboring robot  $j \in \mathcal{N}_i^{\text{robot}}$ . The parameter  $\alpha$  accounts for downwash compensation: in 3D scenarios,  $\alpha = 0$  for the  $x$ - and  $y$ -directions, while  $\alpha > 0$  for the  $z$ -direction. The constant  $\kappa_2$  is a positive control gain and the function  $\mu(s)$  is defined as  $\frac{1}{s} - 1$  for  $s \leq 1$  and 0 otherwise. An example is shown in Fig. 2(c), where robots 4, 10, and 11 are repelled by each other.

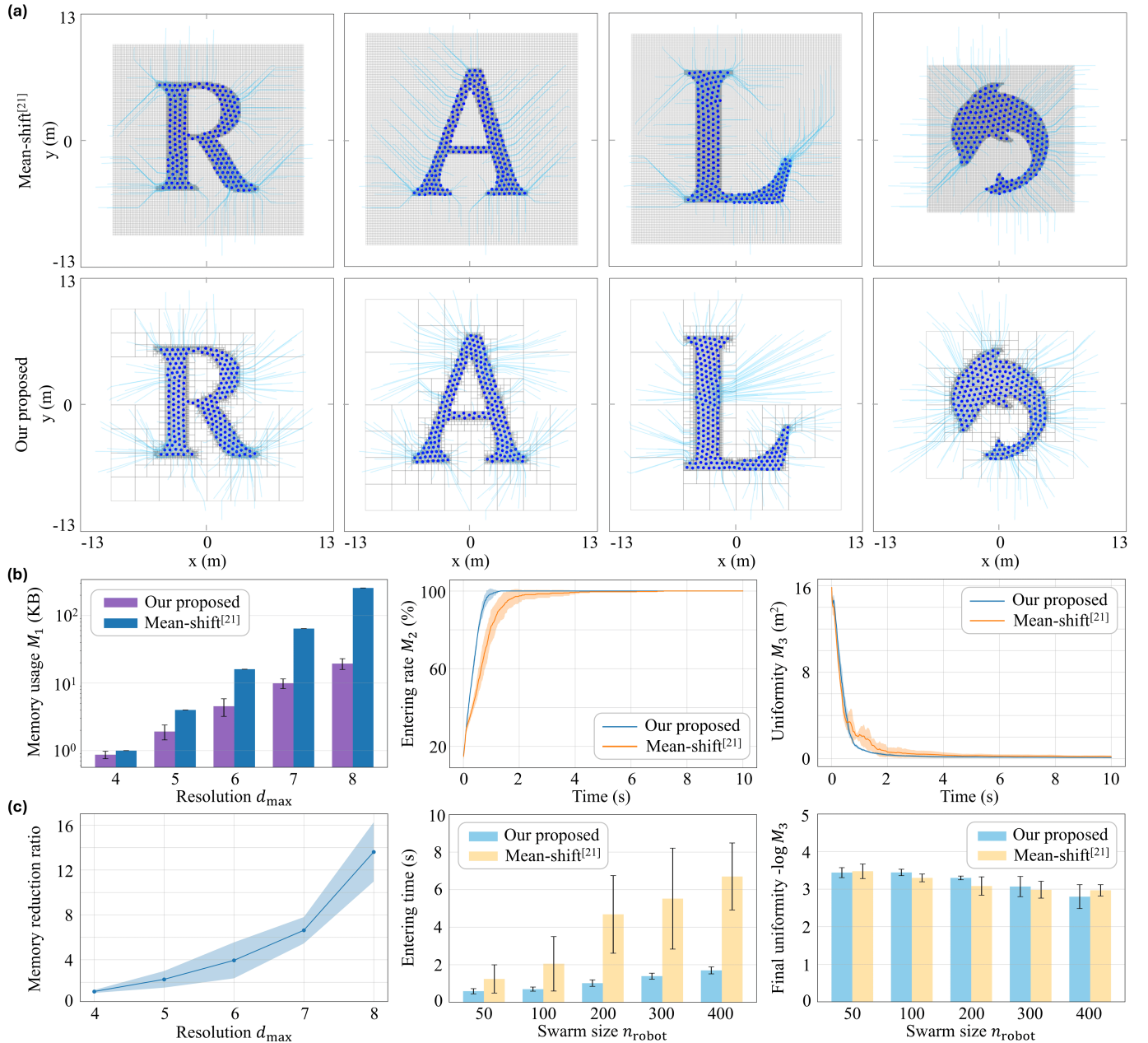


Fig. 3. 2D Simulation Results. (a) Robot trajectories for four target shapes with  $n_{\text{robot}} = 200$ . The first row shows baseline results using full-grid maps (gray-scale omitted for clarity), and the second row shows results of the proposed method with tree maps. (b) Evaluation metrics: memory usage for  $d_{\max}$  from 4 to 8, and entering rate and uniformity over time with  $n_{\text{robot}} = 200$ . (c) Summary of memory reduction ratio, entering time, and final uniformity. The reduction ratio is computed for  $d_{\max} = 4$  to 8, while the other two metrics are evaluated with  $n_{\text{robot}}$  from 50 to 400.

### III. EXPERIMENTS

To evaluate the performance of the proposed shape assembly scheme, both 2D and 3D simulations and physical experiments are conducted, with results shown and analyzed in this section.

#### A. 2D Simulation Results

In the 2D simulation, the proposed scheme is compared with the state-of-the-art Mean-shift algorithm from [21] under identical experimental settings. Robot parameters are set as  $r_{\text{avoid}} = 0.6$  m,  $r_{\text{sense}} = 1.5$  m, and  $v_{\text{max}} = 10$  m/s, while the control parameters are  $\kappa_1 = 20$ ,  $\kappa_2 = 25$ . In the baseline,

$\kappa_1$  governs both entering and exploration, while  $\kappa_2$  handles collision avoidance (see [21] for more details). Both methods use the same resolution:  $d_{\max} = 7$  for the tree map and  $n_{\text{cell}} = 128 \times 128$  for the full-grid map. Both maps are globally decoded at the simulation domain center, with an identical randomly generated initial robot distribution. Simulations run for 1000 time steps with a frequency of 100 Hz. We evaluate four target shapes, including three letters ("R", "A", "L") and one geometry ("Dolphin").

Throughout this section, three quantitative metrics are used for performance evaluation. First, memory usage  $M_1$  quantifies the memory required by the encoded target shapes, which is

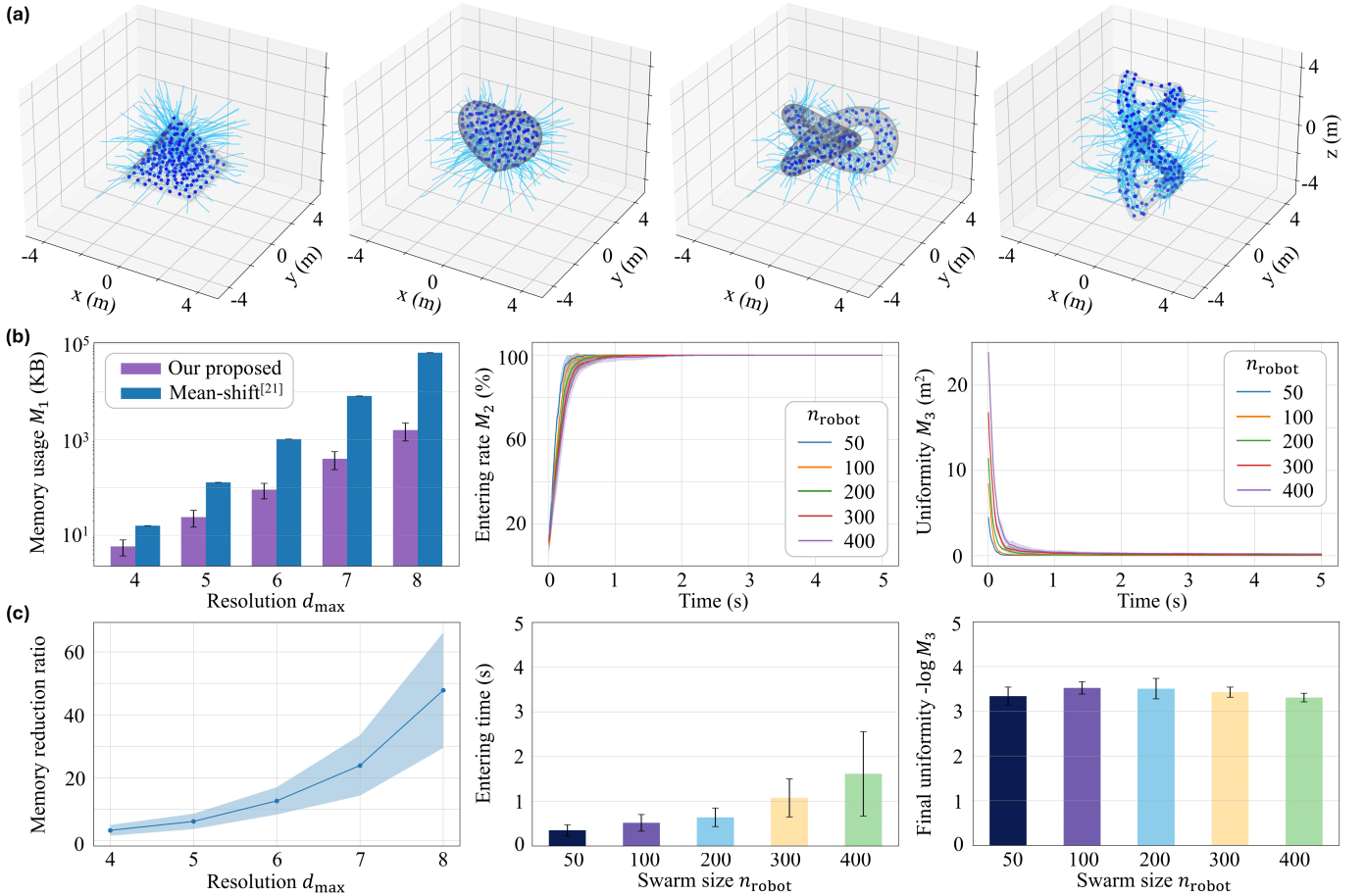


Fig. 4. 3D Simulation Results. (a) Robot trajectories from the proposed method for four target shapes with  $n_{\text{robot}} = 200$ . (b) Evaluation metrics: memory usage for  $d_{\text{max}}$  from 4 to 8, and entering rate and uniformity over time with  $n_{\text{robot}}$  from 50 to 400. (c) Memory reduction ratio, entering time, and final uniformity. The reduction ratio is computed for  $d_{\text{max}} = 4$  to 8, while the other two metrics are evaluated with  $n_{\text{robot}}$  from 50 to 400.

defined in Eqs. 1 and 2 for the proposed and baseline methods, respectively. To enable direct comparison, we further define the memory reduction as the ratio of the baseline’s memory usage to that of the tree map. Second, entering rate  $M_2 = (n_{\text{in}}/n_{\text{robot}}) \times 100\%$ , where  $n_{\text{in}}$  denotes the number of robots located inside the target shape. It measures the proportion of robots that have successfully entered the designated region. The entering time is then defined as the time required for the entering rate to reach 100%. Third, uniformity  $M_3$  evaluates the spatial distribution of robots and is given by  $M_3 = \sum_{i=1}^{n_{\text{robot}}} (r_{\text{min},i} - \bar{r}_{\text{min}})^2$ , where  $r_{\text{min},i} = \min_{j \in \mathcal{N}_{i}^{\text{robot}}} \|\mathbf{p}_i - \mathbf{p}_j\|$  is the minimum inter-robot distance for robot  $i$ , and  $\bar{r}_{\text{min}}$  is the mean of  $r_{\text{min},i}$  across all robots. Ideally, when inter-robot distances are identical,  $M_3 = 0$ . To allow comparisons across different swarm sizes, we define the final uniformity as  $-\log(M_3/n_{\text{robot}})$ , which increases with improved uniformity.

Fig. 3(a) shows the assembled shapes and robot trajectories for the baseline (Mean-shift) and our method with  $n_{\text{robot}} = 200$ . Both algorithms successfully guide the swarm to assemble the desired shapes. To systematically compare performance, Fig. 3(b) presents statistical results based on the three metrics. Since the memory usage is independent of swarm size, it is evaluated with resolutions ranging from  $d_{\text{max}} = 4$  to 8 for all shapes. Entering rate and uniformity

curves are computed using  $n_{\text{robot}} = 200$  over four trials (one per shape). For further comparison, more simulations are performed for all shapes with  $n_{\text{robot}}$  ranging from 50 to 400, with statistical results summarized in Fig. 3(c). The results clearly show the tree map reduces memory usage by a factor of 2 to 16 compared to the full-grid map, with the gap growing exponentially with resolution, as shown in the reduction ratio curve. Despite this reduction, the proposed method achieves similar performance in uniformity: both the convergence speed and final uniformity (around 3 to 4) are close to those of the baseline. Moreover, this uniformity remains stable as swarm size increases from 50 to 400, demonstrating the robustness and scalability of our approach.

The proposed method also achieves markedly higher entering efficiency, reducing entering times by a factor of two to three, with the benefit growing with swarm size. This improvement arises from a key difference in the controller. In the baseline, robots follow local grayscale gradients from distance-based color diffusion, which may deviate from global shortest paths and yield longer trajectories. Sharp shape features can further create gradient valleys that trap robots, causing clustering and queuing. By contrast, our approach employs tree search and coarse-resolution neighboring maps to provide a more global perspective, enabling robots to move

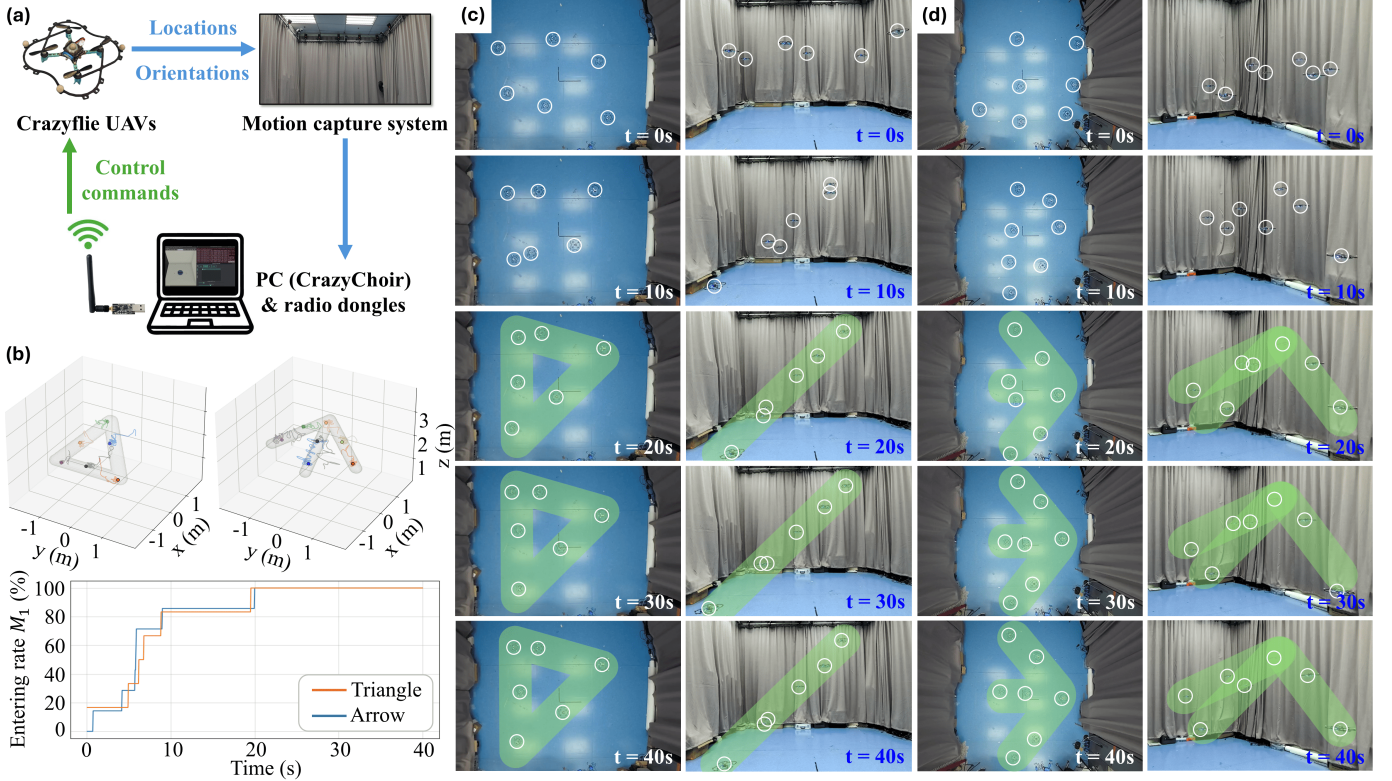


Fig. 5. Physical Experiment Results. (a) Experimental system setup. (b) Robot trajectories and entering rate. Snapshots of the swarm during the experiments of (c) triangle assembly and (d) arrow assembly are shown from two viewing angles.

directly toward the target region without relying on gradient descent. Importantly, such global guidance comes at minimal computational cost, requiring only shallow tree traversal or coarse grid lookup.

### B. 3D Simulation Results

The proposed scheme is also verified in 3D simulations. The baseline is not implemented here since it becomes too time- and memory-consuming in 3D. Compared with 2D simulations, the experimental setting adjustments include parameters  $r_{\text{avoid}} = 0.5$  m,  $r_{\text{sense}} = 0.8$  m,  $\alpha = 0.5$  in the z-direction, and resolution  $d_{\text{max}} = 6$ . All simulations are run for 500 time steps. We select four 3D target shapes: "Pyramid", "Heart", "Knot", and "DNA". Fig. 4(a) shows the final assembled shapes using the proposed algorithm with  $n_{\text{robot}} = 200$  in a 3D view. These results demonstrate that the proposed algorithm can successfully enable a large robot swarm to assemble 3D target shapes, even if for the sophisticated DNA shape.

Fig. 4(b) presents statistical results for all three metrics. For memory usage, we varied the tree depth  $d_{\text{max}}$  from 4 to 8 and compared against the theoretical 3D full-grid map to compute the memory reduction ratio. Entering rate and uniformity curves were obtained from four independent trials (one per shape) with swarm sizes  $n_{\text{robot}}$  ranging from 50 to 400. Fig. 4(c) summarizes the resulting memory reduction ratios, entering times, and final uniformity values. Specifically, the tree map encoding achieves up to 65 times smaller memory at  $d_{\text{max}} = 8$ . Moreover, for every shape and swarm size, the entering rate reaches 100% and the uniformity measure

approaches zero, demonstrating reliable convergence. As  $n_{\text{robot}}$  increases from 50 to 400, the entering time grows only from about 40 to 160 time steps, which indicates an approximately linear scaling. Notably, the mean entering times in 3D closely match those observed in 2D for the same swarm sizes, albeit with greater variation across shapes. Similarly, the final average logarithmic uniformity remains between 3 and 4, which is again consistent with the 2D results. These parallel trends confirm that our algorithm delivers robust, dimension-independent performance.

### C. Physical Experiment Results

In the physical experiment, a 3D triangle and a 3D arrow are assembled by 6 and 7 Crazyflie UAVs, respectively, within a  $4\text{ m} \times 5\text{ m} \times 3\text{ m}$  space, as shown in Fig. 5. The experimental parameters are consistent with those used in the 3D simulations, except for  $r_{\text{sense}} = 1.2$  m,  $v_{\text{max}} = 0.3$  m/s, and  $d_{\text{max}} = 5$ . The system configuration is illustrated in Fig. 5(a), consisting of UAVs, a PC running an open-source aerial swarm control toolbox (CrazyChoir) [29], radio dongsles connected to the PC, and a motion capture system. Considering the instability of peer-to-peer communication among robots, the PC is added to receive real-time robot state information from the motion capture system and execute the proposed algorithm in a distributed manner to compute the control commands. The control commands are then transmitted to the UAVs via the radio dongsles at a control frequency of 20 Hz. Such an experimental setup is commonly used for validating distributed algorithms in physical multi-robot systems [21], [30].

During the experiments, all UAVs first take off and hover at approximately 1 m, then the control algorithm is activated and executed for 40 s. Note that the times reported in this figure refer only to the control phase, excluding take-off and hovering. Fig.5(b) shows the recorded trajectories of all robots and the entering rate curves for the two shapes. In both experiments, all robots enter the shape after approximately 20 s. The corresponding snapshots from the top and oblique side views are presented in Fig.5(c) and (d). The snapshots show that both shapes are assembled within 30 s and maintained until 40 s. The discrepancy between the experimental and simulation assembly efficiency arises mainly from differences in maximum velocity constraints and control frequency due to hardware limitations, as well as real-world system dynamics such as downwash and ground effects. These results demonstrate that the UAV swarm can assemble different target shapes efficiently and robustly, thereby validating the real-world applicability of the proposed algorithm.

#### IV. CONCLUSION

This letter has presented a novel framework for robot swarm shape assembly in both 2D and 3D scenarios. The proposed framework integrated a memory-efficient, tree-based shape encoding-decoding scheme with a behavior-based, distributed assembly controller. Compared with a state-of-the-art image-based baseline, our approach reduced memory usage by one to two orders of magnitude, which is critical for fully distributed systems and resource-constrained robots. Furthermore, 2D and 3D simulations with up to 400 robots demonstrated dimension-independent performance, achieving two to three times faster shape entry while maintaining comparable final uniformity relative to the baseline. Finally, experiments with a swarm of 6 to 7 UAVs validated the practical feasibility of our framework. Future research will focus on eliminating the global frame assumption, reducing dependency on the motion capture system, and developing robust communication strategies to cope with intermittent links in 3D deployments.

#### REFERENCES

- [1] H. F. McCreery, G. Gemayel, A. I. Pais, S. Garnier, and R. Nagpal, "Hysteresis stabilizes dynamic control of self-assembled army ant constructions," *Nature communications*, vol. 13, no. 1, p. 1160, 2022.
- [2] N. Nedjah, G. B. Ferreira, and L. de Macedo Mourelle, "Swarm robotics for collaborative object transport using a pushing strategy," *Expert Systems with Applications*, vol. 271, p. 126610, 2025.
- [3] A. Nitti, M. D. de Tullio, I. Federico, and G. Carbone, "A collective intelligence model for swarm robotics applications," *Nature Communications*, vol. 16, no. 1, p. 6572, 2025.
- [4] K. Zhang, P. Chermprayong, F. Xiao, D. Tzoumanikas, B. Dams, S. Kay, B. B. Kocer, A. Burns, L. Orr, T. Alhinai *et al.*, "Aerial additive manufacturing with multiple autonomous robots," *Nature*, vol. 609, no. 7928, pp. 709–717, 2022.
- [5] R. K. Ramachandran, Z. Kakish, and S. Berman, "Information correlated lévy walk exploration and distributed mapping using a swarm of robots," *IEEE Transactions on Robotics*, vol. 36, no. 5, pp. 1422–1441, 2020.
- [6] M. A. Kamel, X. Yu, and Y. Zhang, "Formation control and coordination of multiple unmanned ground vehicles in normal and faulty situations: A review," *Annual reviews in control*, vol. 49, pp. 128–144, 2020.
- [7] M. Krizmancic, B. Arbanas, T. Petrovic, F. Petric, and S. Bogdan, "Co-operative aerial-ground multi-robot system for automated construction tasks," *IEEE Robotics and Automation Letters*, vol. 5, no. 2, pp. 798–805, 2020.
- [8] D. Morgan, G. P. Subramanian, S.-J. Chung, and F. Y. Hadaegh, "Swarm assignment and trajectory optimization using variable-swarm, distributed auction assignment and sequential convex programming," *The International Journal of Robotics Research*, vol. 35, no. 10, pp. 1261–1285, 2016.
- [9] M. Turpin, N. Michael, and V. Kumar, "Capt: Concurrent assignment and planning of trajectories for multiple robots," *The International Journal of Robotics Research*, vol. 33, no. 1, pp. 98–112, 2014.
- [10] X. Shan, Y. Jin, M. Jurt, and P. Li, "A distributed multi-robot task allocation method for time-constrained dynamic collective transport," *Robotics and Autonomous Systems*, vol. 178, p. 104722, 2024.
- [11] Y. Liu and Z. Liu, "Distributed adaptive formation control of multi-agent systems with measurement noises," *Automatica*, vol. 150, p. 110857, 2023.
- [12] O. Shorinwa, R. N. Haksar, P. Washington, and M. Schwager, "Distributed multirobot task assignment via consensus admn," *IEEE Transactions on Robotics*, vol. 39, no. 3, pp. 1781–1800, 2023.
- [13] K. Sakurama and H.-S. Ahn, "Multi-agent coordination over local indexes via clique-based distributed assignment," *Automatica*, vol. 112, p. 108670, 2020.
- [14] S. Zhao and D. Zelazo, "Bearing rigidity theory and its applications for control and estimation of network systems: Life beyond distance rigidity," *IEEE Control Systems Magazine*, vol. 39, no. 2, pp. 66–83, 2019.
- [15] K. Li, Z. Ma, L. Li, and S. Zhao, "Collective behavior clone with visual attention via neural interaction graph prediction," *arXiv preprint arXiv:2503.06869*, 2025.
- [16] H. Wang and M. Rubenstein, "Shape formation in homogeneous swarms using local task swapping," *IEEE Transactions on Robotics*, vol. 36, no. 3, pp. 597–612, 2020.
- [17] M. Rubenstein, A. Cornejo, and R. Nagpal, "Programmable self-assembly in a thousand-robot swarm," *Science*, vol. 345, no. 6198, pp. 795–799, 2014.
- [18] I. Slavkov, D. Carrillo-Zapata, N. Carranza, X. Diego, F. Jansson, J. Kaandorp, S. Hauert, and J. Sharpe, "Morphogenesis in robot swarms," *Science Robotics*, vol. 3, no. 25, p. eaau9178, 2018.
- [19] L. Sabattini, C. Secchi, and C. Fantuzzi, "Arbitrarily shaped formations of mobile robots: artificial potential fields and coordinate transformation," *Autonomous Robots*, vol. 30, no. 4, pp. 385–397, 2011.
- [20] M. Alhafnawi, S. Hauert, and P. O'Dowd, "Self-organised saliency detection and representation in robot swarms," *IEEE Robotics and Automation Letters*, vol. 6, no. 2, pp. 1487–1494, 2021.
- [21] G. Sun, R. Zhou, Z. Ma, Y. Li, R. Groß, Z. Chen, and S. Zhao, "Mean-shift exploration in shape assembly of robot swarms," *Nature Communications*, vol. 14, no. 1, p. 3476, 2023.
- [22] Y. Zhang, R. Zhou, X. Li, and G. Sun, "Mean-shift shape formation of multi-robot systems without target assignment," *IEEE Robotics and Automation Letters*, vol. 9, no. 2, pp. 1772–1779, 2024.
- [23] J. Lü, K. Ze, S. Yue, K. Liu, W. Wang, and G. Sun, "Concurrent-learning based relative localization in shape formation of robot swarms," *IEEE Transactions on Automation Science and Engineering*, 2025.
- [24] F. Berlinger, M. Gauci, and R. Nagpal, "Implicit coordination for 3d underwater collective behaviors in a fish-inspired robot swarm," *Science Robotics*, vol. 6, no. 50, p. eabd8668, 2021.
- [25] K. Cabral, T. Kaykobad, J.-A. Delamer, P. Jardine, and S. Givigi, "Design of a decentralized strategy for layered self-assembly of 3d structures using robotic blocks," *Journal of Intelligent & Robotic Systems*, vol. 107, no. 4, p. 54, 2023.
- [26] P. Swisser and M. Rubenstein, "Fireant3d: a 3d self-climbing robot towards non-latticed robotic self-assembly," in *2020 IEEE/RSJ International Conference on Intelligent Robots and Systems (IROS)*. IEEE, 2020, pp. 3340–3347.
- [27] L. Zhao, Y. Jiang, M. Chen, K. Bekris, and D. Balkcom, "Modular shape-changing tensegrity-blocks enable self-assembling robotic structures," *Nature Communications*, vol. 16, no. 1, p. 5888, 2025.
- [28] L. Zhao, Y. Jiang, C.-Y. She, M. Chen, and D. Balkcom, "Softsnap: Rapid prototyping of untethered soft robots using snap-together modules," *Soft Robotics*, 2025.
- [29] L. Pichierri, A. Testa, and G. Notarstefano, "Crazychoir: Flying swarms of crazyflie quadrotors in ros 2," *IEEE Robotics and Automation Letters*, vol. 8, no. 8, pp. 4713–4720, 2023.
- [30] D. Mulroy, E. Lopez, M. Spenko, and A. Srivastava, "Using r-functions to control the shape of soft robots," *IEEE Robotics and Automation Letters*, vol. 7, no. 4, pp. 8598–8603, 2022.